THE ASTROPHYSICAL JOURNAL, 275:652–660, 1983 December 15


# SHOCK PROCESSING OF INTERSTELLAR GRAINS

C. GREGORY SEAB[1]
Department of Physics, University of Colorado, and Laboratory for Atmospheric and Space Physics
AND
J. MICHAEL SHULL
Joint Institute for Laboratory Astrophysics, University of Colorado and National Bureau of Standards, and Laboratory for Atmospheric and Space Physics
*Received 1983 February 14; accepted 1983 May 17*

## ABSTRACT

We present theoretical and observational evidence that shock processing of interstellar dust grains by supernova blast waves affects both heavy element depletions and ultraviolet extinction curves. By coupling a realistic model of grain sizes and populations with a radiative shock code, we demonstrate significant grain destruction at velocities as low as 40 km $s^{-1}$. Nonthermal sputtering and grain-grain collisions destroy relatively more large grains than small, and more silicates than graphite. Consequently, both the 2175 Å extinction "bump" and the far-ultraviolet normalized extinction are increased in strength. Ultraviolet extinction studies with the *International Ultraviolet Explorer* of nine stars near three supernova remnants (the Monoceros Loop, Shajn 147, and Vela) exhibit strong 2175 Å bumps and normal or high far-ultraviolet extinction. Diffuse bands, if they are created by small grains, should show little correlation with such activity.

*Subject headings:* interstellar: grains — nebulae: supernova remnants — shock waves — ultraviolet: spectra

## I. INTRODUCTION

The emerging picture of grains in the interstellar medium is more complex than early observations indicated. Although Nandy *et al.* (1976) found that the grain extinction curve in the ultraviolet was fairly uniform in most directions, significant variations have recently been seen in dense clouds and young clusters, as well as in lines of sight with no obvious nebulosity (Meyer and Savage 1981).

The correlation between extinction anomalies and other measures of the interstellar medium are weak and rare, implying that a number of different processes affect the extinction properties of the grains, probably with different results. In this paper we consider the extinction properties of grains that have been processed by the shock waves mediating the dynamics and thermal phases of the "violent interstellar medium" (McKee and Ostriker 1977; McCray and Snow 1979).

To study the grain processing, we employ a modification of the most realistic grain population model currently available (Mathis, Rumpl, and Nordsieck 1977, hereafter MRN), combined with a hydrodynamic radiative shock code (Shull and McKee 1979). The gradual destruction of grains in the postshock region increases the gas-phase abundances of refractory elements normally locked up in the grains, increasing in turn the cooling of the postshock gas and altering the shock structure. This nonlinear interaction between the grains and gas has been incorporated into the shock code (Shull, Seab, and McKee 1983).

In the following sections we describe the features of the grain model (§ II), the shock code (§ III), and the results of the models (§ IV). In § V we discuss the results and compare them to observations of extinction toward stars behind supernova remnants (SNRs), and in § VI we present a summary.

## II. GRAIN MODEL

The best available grain model (MRN) attributes the 2175 Å extinction feature to graphite grains and adds silicate grains to reproduce the observed normal extinction curve, $E(\lambda - V)/E(B - V)$, from the far-infrared to the far-ultraviolet. For the purposes of this project, some modifications are required to balance the MRN grain model with the observed heavy element depletions in the interstellar medium. While the resulting theoretical extinction curve differs slightly from the observed normal extinction curve, we will only be concerned with relative changes.

The well-studied $\zeta$ Oph line of sight (Morton 1974, 1975) was used as a guide to the preshock abundances,

[1]Guest Investigator on NASA's *International Ultraviolet Explorer* (*IUE*) Telescope.

with most heavy elements depleted into grains. Graphite grains were retained in a pure state, and essentially all the observed depletion of Fe and Mg was accounted for by a mixture of about 75% olivine ([Mg, Fe] $SiO_4$) and 25% enstatite ([Mg, Fe] $SiO_3$). About 58% of this mixture will be the Mg form and the remainder Fe (technically, the Fe forms are fosterite and ferroslite). Since enstatite and olivine have similar optical properties, the use of this mixture will not affect the extinction curves.

Unfortunately, this mixture of silicates does not account for all the elements missing from the gas phase. Nitrogen and sulfur are depleted by about 50% toward $\zeta$ Oph and should be included in grains or molecules. The 25% oxygen depletion is also not entirely accounted for by the silicates. We include N, O, and S with the silicate grains in an indeterminate form, resulting in a 30% increase in the weight of the silicate grains and somewhat increased grain destruction in the shock. The alternative of assuming that these elements are tied up in molecules is not justified by the abundances of the most important molecules toward $\zeta$ Oph (Morton 1975). If these elements exist as volatile ice mantles ($H_2O$, $NH_3$, etc.), they would sputter early in the shock. However, in the diffuse interstellar medium, grains are unlikely to develop substantial mantles in lines of sight with $E(B-V)<1.0$ in a single cloud (Harris, Woolf, and Rieke 1978).

The optical constants for the indeterminate portion of the grain mix are unknown, and we have simply applied the constants appropriate for the silicate portion to the entire grain. Since only relative changes in the extinction curve are sought, the results should be minimally affected. Table 1 shows the final choice of elements for the grain mixture, normalized to one silicon atom. Carbon is included in the table for reference, but is considered in a separate graphite grain population.

The composition of the particle sputtered from the silicate mixture is also uncertain. We assume that each sputtering event releases the equivalent of a complete molecule, as evidenced by data for $SiO_2$ (Jorgenson and Wehner 1965; Barlow 1978) and in agreement with atom-by-atom sputtering data discussed by Draine and Salpeter (1979). As a molecular weight, we assume an appropriate average of the Mg and Fe forms of enstatite and olivine. To account for N, O, and S, we assign the average sputtered silicate particle 0.769 of a silicate unit crystal by mass, with the remainder made up of the additional elements. The final selections for the grain parameters are given in Table 2.

TABLE 1

GRAIN COMPOSITION

| Element | Cosmic Abundance[a] | Depletion[b] | X/Si[c] |
|---|---|---|---|
| C | 3.70(−4) | 0.80 | ... |
| N | 1.15(−4) | 0.50 | 1.67 |
| O | 6.76(−4) | 0.25 | 4.91 |
| Mg | 3.47(−5) | 0.97 | 0.98 |
| Si | 3.55(−5) | 0.97 | 1.00 |
| S | 1.58(−5) | 0.44 | 0.20 |
| Fe | 2.51(−5) | 0.98 | 0.71 |

[a]Abundances by number, relative to H (Morton 1974).
[b]Number fraction of element contained in grains.
[c]Fractional number abundance in grains relative to Si = 1.00.

TABLE 2

SPUTTERING PARAMETERS[a]

| Parameter | Graphite | Silicate |
|---|---|---|
| $H_s$(eV) | 7.35 | 4.50 |
| $M_{sp}(m_H)$ | 12 | 154 |
| $V_{th}$(km s$^{-1}$) | 13.3 | 5.1 |
| $\rho_{gr}$(g cm$^{-3}$) | 2.2 | 3.2 |

[a]Sublimination energy ($H_s$), total mass of sputtered particles ($M_{sp}$), grain density ($\rho_{gr}$), and threshold velocity ($V_{th}$) for grain-grain destruction.

The size distribution of the grains follows the power law,

$$n_i(R)\,dR = K_i R^{-3.5}\,dR, \qquad (1)$$

for grains between 0.01 and 0.25 $\mu$m, divided into 25 logarithmically spaced bins. The constants $K_i$ were determined by normalizing the total number of carbon or silicon atoms to the desired depletion factor from Table 2. Extinction curves were calculated for the grain model by standard Mie theory (van de Hulst 1957), using optical constants kindly supplied by Dr. John Mathis. Figure 1 compares the model extinction curve (used to compare shock processing results) to the standard observed curve for the normal interstellar medium (Savage and Mathis 1979). The model curve lies somewhat higher than the standard, primarily because we assumed the silicate optical constants for the indeterminate portion of the grain mixture.

Most previous calculations of grain destruction (e.g., Shull 1977, 1978; Cowie 1978; Draine and Salpeter 1979) have been performed for only one grain type at a time. This leads to an underestimate of the grain-grain destruction, since it excludes collisions between grains of different varieties and sizes. Thus, the present model, even with its approximations and assumptions, will give more realistic results.

## III. COMPUTER CODE

The basic shock code is essentially that of Shull and McKee (1979), modified as described in Shull, Seab, and McKee (1983). the salient features of the code are as follows. The shock is treated as a one-dimensional, plane-parallel hydrodynamical flow, with nonequilib-

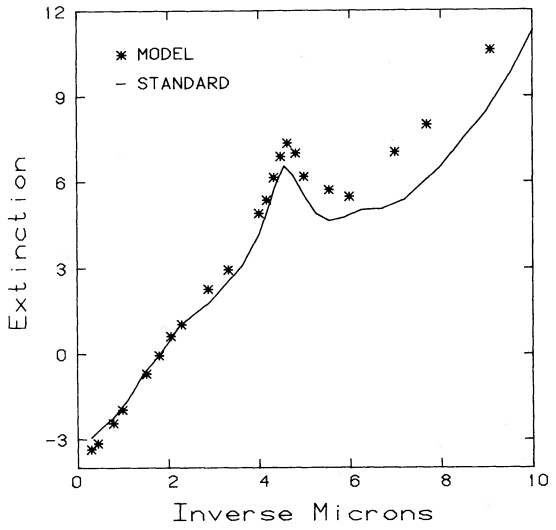


FIG. 1.—Comparison of initial model extinction, $E(\lambda - V)/E(B-V)$, with the standard curve (Savage and Mathis 1979).

rium radiative cooling in the postshock region. The jump conditions at the adiabatic shock front are those of Hollenbach and McKee (1979), including a perpendicular magnetic field. The time-dependent populations of various ionization stages of H, He, C, N, O, Ne, Si, S, and Fe are calculated for collisional and radiative ionization, radiative and dielectronic recombination, and charge exchange with H I and He I. Cooling rates are calculated for line emission, two-photon emission, bremsstrahlung, and recombination continua. Approximate radiative transfer calculations are done in both the upstream and downstream directions. The initial ionization stages are set by calculations of the radiative precursor to the shock, so that a self-consistent solution is obtained after iteration. In practice, only two or three iterations were necessary for convergence in the precursor ionization levels and the shock structure.

The primary changes in the shock code are the addition of Ne and Fe and the allowance for variable element depletions resulting from grain destruction. The physics of grain destruction follows the formalism of Shull (1977, 1978). Nonthermal grain sputtering is calculated from the formula (Barlow 1978) for the yield,

$$y(E) = (3.2\times10^{-3})(E - E_T)/E_T, \quad E_T = 4H_s, \quad (2)$$

where $y(E)$ is the yield in sputtered particles for a collision energy $E$; $E_T$ is the threshold energy for sputtering, approximately equal to 4 times the heat of sublimation $H_s$. Draine and Salpeter (1979) comment that this formula fits experimental data at low energies approximately as well as their formula. At high energies, they advocate a different formulation by Sigmund (1969), which has a gradually decreasing yield. This transition will be approximated by limiting the effective projectile energy to 200 eV for silicates and 300 eV for graphite. A flat sputtering yield above these energies fits the experimental data over the range of energies of interest (Draine and Salpeter 1979, Fig. 3) as well as Sigmund's formula. Because helium dominates the nonthermal sputtering, we neglect H collisions.

Thermal sputtering was included according to Barlow (1978, eq. [1]),

$$dR/dt = (2n_{\rm H}M_{\rm sp}/\rho_{\rm gr})(kT/2\pi m_{\rm H})^{1/2}(kTS_{\rm H}/H_s) \times (4H_s/kT + 2)\exp(-4H_s/kT), \quad (3)$$

where $R$ is the grain radius, $\rho_{\rm gr}$ the grain mass density, $H_s$ the heat of sublimation, $M_{\rm sp}$ the mass of a sputtered particle, $n_{\rm H}$ and $m_{\rm H}$ the hydrogen number density and mass, and $S_{\rm H}$ the sputtering yield constant. Thermal sputtering was found to be small compared with other grain destruction mechanisms, approaching 10% of the nonthermal rates only in the immediate postshock layer.

We modified the treatment of grain-grain collisions in Shull (1978) to account for grains of different sizes and compositions. The starting point is the relation,

$$df_1/dt = \alpha\langle n_2\sigma_{12}v_{12}\rangle, \quad (4)$$

where $f_1$ is the fraction of "test" grains destroyed, $n_2$ is the number density of colliding "field" grains, $\sigma_{12} = \pi(R_1 + R_2)^2$ is the collision cross section for grains of radii $R_1$ and $R_2$, $v_{12}$ is the relative approach velocity, and $\alpha$ is a correction factor to account for the less effective grazing encounters. We set $\alpha = 0.5$.

For an approach angle $\Psi$ between the colliding grains, the relative velocity is just given by the cosine law. Averaging over all approach angles gives

$$\langle v_{12}\rangle = \frac{1}{\pi}\int_{\Psi_{\rm cr}}^{\pi}(v_1^2 + v_2^2 - 2v_1v_2\cos\Psi)^{1/2}\,d\Psi. \quad (5)$$

The integral can be evaluated as an elliptic integral of the second kind:

$$\langle v_{12}\rangle = \frac{2}{\pi}(v_1 + v_2)E(k, \phi_{\rm cr}),$$

$$k = \frac{4v_1v_2}{(v_1 + v_2)^2}, \quad \phi_{\rm cr} = \frac{\pi - \Psi_{\rm cr}}{2}, \quad (6)$$

where $\Psi_{\rm cr}$ is the critical angle between trajectories for which the collision is energetic enough for grain disruption. For destruction of both particles,

$$\cos(\Psi_{\rm cr}) = \frac{1}{2\mu v_1v_2}\left[\mu(v_1^2 + v_2^2) - m_1v_{1t}^2 - m_2v_{2t}^2\right], \quad (7)$$

where $\mu$ is the reduced mass and $v_{it} \equiv (2E_{\rm bind}/M_{\rm sp})^{1/2}$ are the threshold velocities ($i=1,2$) for disruption ($E_{\rm bind} \approx 1.5H_s$). For the destruction of only one of the particles, the appropriate threshold energy term is omitted.

In dealing with collisions between particles of widely disparate masses, it is necessary to consider what happens when the collision energy is sufficient to destroy one of the particles, but not both. The outcome will depend on the collision energy and may range from elastic scattering or coagulation of the particles at very low energies to total vaporization at high energies. Between these extremes, fragmentation or partial vaporization might occur. Some aspects of fragmentation have been discussed by Biermann and Harwit (1980), who note that this process could lead to a $-3.5$ index power-law size spectrum, as in the MRN grain model. Detailed consideration of grain fragmentation is beyond the scope of this present project. If fragmentation were a dominant process, then the amount of grain destruction in shocks would be greatly decreased, contrary to observation (Shull, York, and Hobbs 1977, and references therein).

We therefore simplify the problem by considering only total vaporization of one or both particles. In classical mechanics, an elastic collision between two particles of unequal weight always leaves the lighter particle with most of the collision energy. (If the weights differ by only a factor of 2, then more than 90% of the energy is deposited with the less massive particle.) This principle motivates us to assume that the lighter of the two grains will be vaporized first, and the heavier grain will vaporize only if enough energy is left over. This assumption will approximate a collision in which some partial vaporization occurs.

The equation of motion of the grain is taken from Shull (1978):

$$\frac{dV_{\rm gr}}{dt} = \frac{V_{\rm gr}}{2B}\frac{dB}{dt} - \frac{\pi R^2}{M_{\rm gr}}\rho V_{\rm gr}^2 - \frac{F_{\rm pl}}{M_{\rm gr}}, \qquad (8)$$

where $V_{\rm gr}$ is the gyrovelocity of a grain of mass $M_{\rm gr}$ and radius $R$, $B$ is the magnetic field strength, $\rho$ is the gas density, and $F_{\rm pl}$ is a plasma drag term, dependent on the grain charge $Z_{\rm gr}$. The first term on the right is the betatron acceleration term in the small Larmor radius approximation (Spitzer 1976; Shull 1977), and the next two terms give the collisional and plasma drag decelerations. The betatron acceleration is largely responsible for the amount of grain destruction, since it increases the gyrovelocity of the grain without allowing it to escape; the guiding center continues to drift with the gas flow. Plasma drag is most effective when the grain is slowing down; it causes the velocities to drop abruptly below sputtering thresholds.

The small Larmor radius approximation will break down for very large grains or for shocks with short cooling lengths. If the Larmor radius,

$$R_{\rm L} = \frac{M_{\rm gr}V_{\rm gr}c}{Z_{\rm gr}eB}, \qquad (9)$$

is very much larger than the cooling length of the shock, then the grain will pass through the shock layers without much disruption. For the passage of such a particle through a 100 km s$^{-1}$ shock, the fraction $f$ of grains colliding with the confined grains can be estimated from the cooling time $t_c$ as

$$f = t_c\langle n_{\rm gr}\sigma_{\rm gr}V_{\rm gr}\rangle \approx \frac{L_c}{V_{\rm gr}}\left[\sum_i n_i\pi(R_i + R_{\rm gr})^2\right]V_{\rm gr} = 5\times10^{-4}, \qquad (10)$$

where the summation is over the grain sizes, evaluated for the standard model, $R_{\rm gr} = 2.5\times10^{-5}$ cm, and a cooling length $L_c \approx 5.0\times10^{15}$ cm. Thus a grain massive enough to have $R_{\rm L} \gg L_c$ will be largely unscathed by its passage through the shock. Deceleration in the denser medium downstream of the shock will prevent its return to the shock layers.

An exact solution of the grain trajectory would require detailed calculations of its orbit through the shock layers. We make the simplifying assumption that the betatron acceleration formalism is applicable for grains with $R_{\rm L} < L_c$, while larger grains are unaffected by the shock. For the 100 km s$^{-1}$ standard case, the typical $R_{\rm L}$ for the largest silicate grains is about half the cooling length. For much larger grains or higher gas densities this assumption might break down.

## IV. RESULTS

Table 3 gives the parameters for the shock processing models. The density and magnetic field values refer to the preshock medium. The standard grain parameters are given in Tables 1 and 2; only variations are listed in Table 3. A number of additional cases not involving grain destruction were run but are not listed here. Full results on these cases plus details of the shock structure, continuum emission, and line strengths will be given in a forthcoming paper (Shull, Seab, and McKee 1983).

The shock structure in the grain-processing models falls between the undepleted case and the depleted case without grain processing. Figure 2 shows the temperature structure of the shock for models 100A, 100B, and 100C. Model 100A is the standard grain-processing model with a velocity of 100 km s$^{-1}$. It follows model 100C fairly well until the additional cooling from grain destruction takes effect. Note that a step in the temper-

TABLE 3

SHOCK MODELS

| Model | $V_s$ (km s$^{-1}$) | $n_0$ (cm$^{-3}$) | $B_0$ (gauss) | Grains[a] |
|---|---|---|---|---|
| 100A..... | 100 | 10. | $10^{-6}$ | standard |
| 100B..... | 100 | 10. | $10^{-6}$ | undepleted |
| 100C..... | 100 | 10. | $10^{-6}$ | depleted, no grains |
| 100D .... | 100 | 100. | $10^{-6}$ | standard |
| 100E..... | 100 | 10. | $5\times10^{-6}$ | standard |
| 100F..... | 100 | 10. | $10^{-6}$ | $\rho_{Sil} = 2.5$ |
| 100G .... | 100 | 10. | $10^{-6}$ | $M_{sp} = 104$ (Sil.) |
| 100H .... | 100 | 10. | $10^{-6}$ | $H_s = 5.7$ eV (Sil.) |
| 120 ..... | 120 | 10. | $10^{-6}$ | standard |
| 110 ..... | 110 | 10. | $10^{-6}$ | standard |
| 80 ..... | 80 | 10. | $10^{-6}$ | standard |
| 60 ..... | 60 | 10. | $10^{-6}$ | standard |
| 40 ..... | 40 | 10. | $10^{-6}$ | standard |

[a]Grain parameters: standard refers to Table 2; exceptions as noted.

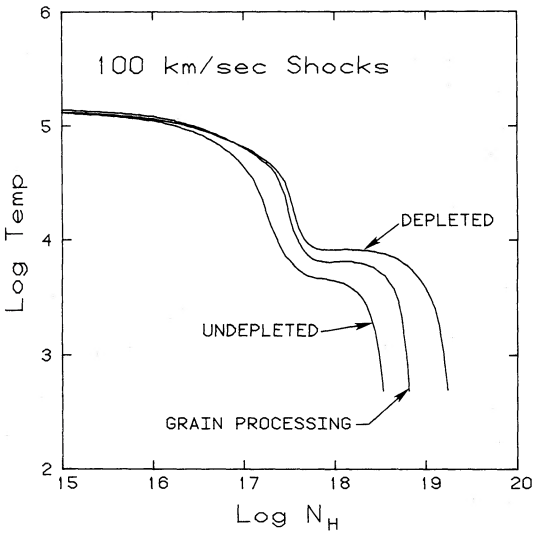


FIG. 2.—Shock temperature structure for 100 km s$^{-1}$ shock models 100B (undepleted, no grain destruction), 100A (depleted, with grain processing included), and 100C (depleted, but no grain processing). The horizontal axis is labeled by $N_H$, the total column density (cm$^{-2}$) of hydrogen measured downstream from the shock front.

ature curves occurs in the hydrogen recombination zone ($T \sim 6000$ K).

The principal result of this project is the set of extinction curves shown in Figure 3. The normalized shock-processed extinction curves lie above the standard throughout the ultraviolet. Both the 2175 Å bump strength and the far-ultraviolet normalized extinction are increased. This can be understood as a combination of two effects. First, the silicate grains suffer more destruction than the graphite grains. Table 4 lists the fractional abundances of the elements in the gas phase, relative to their cosmic abundance. For all models, carbon starts out with 20% in the gas phase and never gets over 35% after shock processing. But more than half of the silicate grain material is returned to the gas phase. This causes the graphite extinction feature at 2175 Å to be strengthened relative to the rest of the curve.

The second effect is due to the greater destruction of large grains than of small grains. Figure 4 shows the size distribution of silicate grains before and after the 100A model shock. Over 50% of the largest grains have been destroyed by grain-grain collisions, while virtually all of the smallest grains are intact. The remaining large grains are also reduced to about 75% of their initial radius, while the smallest ones are nearly unchanged. Since the larger grains absorb more efficiently in the visual range,

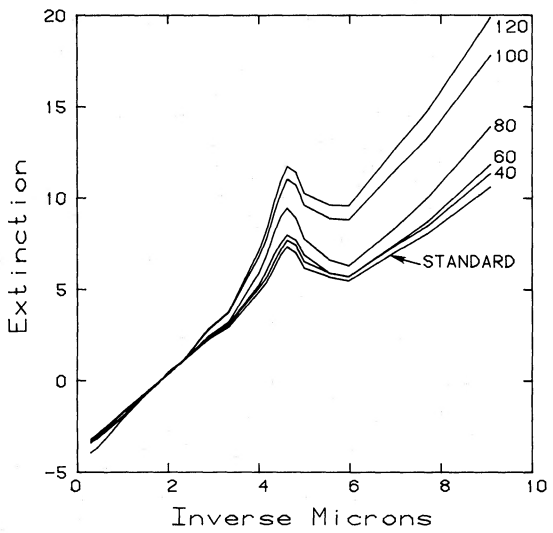


FIG. 3.—Normalized $E(\lambda - V)/E(B - V)$ extinction curves for five shock velocities (km s$^{-1}$). The lowest curve represents the preshock standard.

TABLE 4

POSTSHOCK GAS-PHASE FRACTIONAL ABUNDANCE[a]

| Model | C | N | O | Si | S | Fe |
|---|---|---|---|---|---|---|
| INIT .... | 0.20 | 0.50 | 0.75 | 0.03 | 0.56 | 0.02 |
| 100A .... | 0.28 | 0.76 | 0.88 | 0.54 | 0.79 | 0.53 |
| 100D .... | 0.29 | 0.79 | 0.90 | 0.58 | 0.81 | 0.58 |
| 100E .... | 0.24 | 0.70 | 0.85 | 0.41 | 0.73 | 0.40 |
| 100F .... | 0.28 | 0.74 | 0.87 | 0.50 | 0.77 | 0.50 |
| 100G .... | 0.27 | 0.72 | 0.86 | 0.46 | 0.76 | 0.46 |
| 100H .... | 0.25 | 0.71 | 0.85 | 0.44 | 0.75 | 0.43 |
| 120..... | 0.32 | 0.79 | 0.90 | 0.60 | 0.82 | 0.59 |
| 110..... | 0.30 | 0.77 | 0.89 | 0.56 | 0.80 | 0.55 |
| 80..... | 0.27 | 0.72 | 0.86 | 0.45 | 0.75 | 0.45 |
| 60..... | 0.24 | 0.70 | 0.85 | 0.41 | 0.73 | 0.40 |
| 40..... | 0.22 | 0.56 | 0.79 | 0.17 | 0.63 | 0.17 |

[a]Fractional abundances of heavy elements in gas phase: INIT (preshock depletion), models 100A–H, etc. (Table 3), refer to postshock conditions after grain processing.

the $E(B-V)$ reddening will be disproportionately lowered. Normalizing to $E(B-V)$ then has the effect of raising the entire curve. The shock-processed extinction curves would be lower than the standard if normalized to a hydrogen column density $N(\mathrm{H_{tot}}) = 5.8\times10^{21}$ $\mathrm{cm^{-2}}$, usually corresponding to $E(B-V)=1.0$ (Bohlin, Savage, and Drake 1978).

The combination of a greater destruction of silicate grains than of graphite grains, plus the greater destruction of large grains, leads to a characteristic normalized extinction curve with a strong 2175 Å feature, a high far-ultraviolet extinction, and a high ratio $N(\mathrm{H_{tot}})/E(B-V)$. The ratio, $R = A_v/E(B-V)$, of total to selective extinction is also affected slightly, increasing from 3.7 (standard model or low velocity) to 3.9 ($V_s > 100$ km $\mathrm{s^{-1}}$).

Figure 5 shows the velocity structure of the largest and smallest grains of both graphite and silicate for the 100A case. The betatron acceleration is independent of the mass of the grain in the small Larmor radius approximation, but the plasma drag and collisional deceleration are more effective for the smaller grains. Therefore, the more massive and dense grains reach much higher velocities and consequently suffer more destruction. The most massive grains increase in gyrovelocity until the compression levels off owing to the decreasing cooling rate and the increased magnetic pressure. Since the betatron acceleration depends on the change in magnetic field, which follows the density, the acceleration will decrease at this point, and the drag quickly brings the grains to a halt. Essentially all the grain destruction takes place near the velocity peak.

The relative efficiency of the destruction processes also depends on the grain size. Grain-grain collisions are more efficient than nonthermal sputtering for the larger grains by factors of 5–10 for the 100A case. For the smaller grains, sputtering dominates by about the same factors. This is the expected relationship, since the

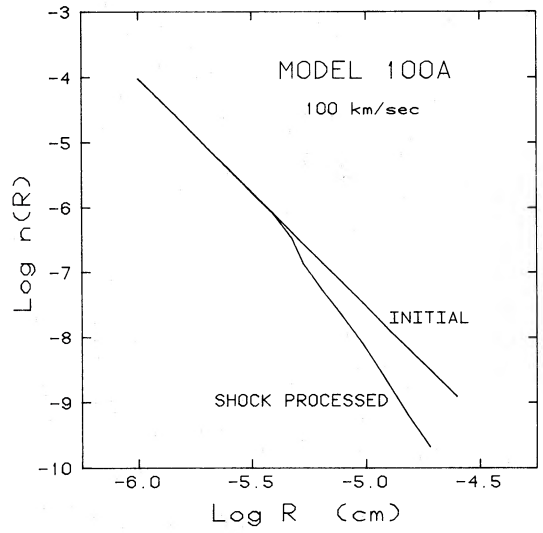


FIG. 4

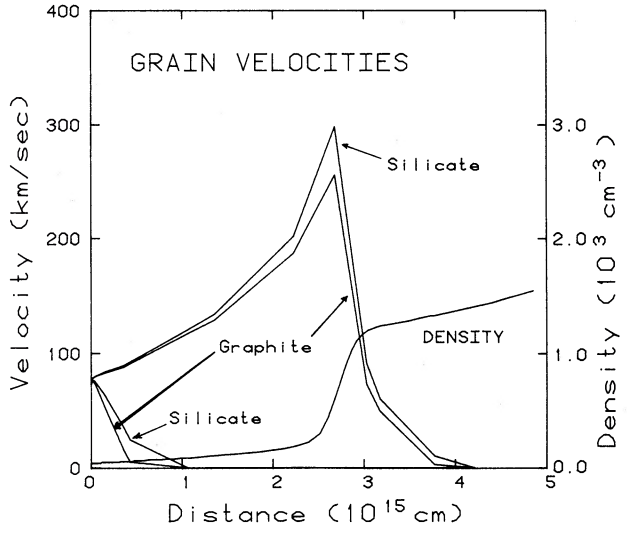


FIG. 5

FIG. 4.—Silicate grain size distribution $n(R)$, for the initial grain model with a power-law index $-3.5$, and for model 100A (100 km $\mathrm{s^{-1}}$) shock-processed grains.

FIG. 5.—Grain velocities for the largest and smallest grains as a function of distance behind a 100 km $\mathrm{s^{-1}}$ shock. The smallest grains decelerate almost immediately, while the gyrovelocities of the largest grains are increased by betatron acceleration, peaking at postshock column density $\log N_{\mathrm{H}} = 17.55$. Also shown is the gas density $n(\mathrm{H})$, directly proportional to the frozen-in magnetic field.

grain-grain collisions depend on the mass, while sputtering depends on the surface area of the grains.

The size distribution was found to be very important in the grain-grain collisions. With $n(R) \sim R^{-3.5}$ from the MRN grain model, the numbers of grains increase rapidly with decreasing size. The energy of the collision decreases with the decreasing mass, but there is still a $R^{-0.5}$ gain in importance for the smaller grains. Much smaller grains travel at lower velocities and do not carry enough energy to be effective in vaporizing the larger grains. We found that grains of a given size were most efficiently destroyed by grains of about half their radius; vaporization did not occur for grains much smaller than this. Grain destruction models that use only one size grain at a time will underestimate the importance of grain-grain collisions.

For all of the models considered here, the Larmor radius was smaller than the cooling length for the largest grains. These grains contain only a few percent of the total grain mass, since the power-law index is steeper than $R^{-3}$. Therefore, the effect of the small Larmor radius approximation on the total amount of destruction will be minimal. The effect on the extinction curve can be approximated by adding the extinction from the largest grains to the postshock extinction and renormalizing. For the 100A case, this procedure showed only a slight decrease in the UV extinction, but an increase in the ratio $R$ of total to selective extinction.

The results of this study depend on the basic validity of the MRN model (i.e., the separation into silicate and graphite components and the identification of graphite as the carrier of the 2175 Å bump.) They are not very sensitive to the particular choice of grain parameters. The postshock percentage of gas-phase silicon in Table 4 varies only from 54% to 40% for different grain parameters. The critical factor is the considerably higher binding energy for graphite grains, which makes them more resistant to destruction. If graphite grains do indeed exist in the interstellar medium and are the source of the 2175 Å extinction bump, then the strength of that feature should be increased by shock processing of the grains.

## V. COMPARISON WITH OBSERVATIONS

*IUE* low-dispersion observations have been made of nine stars (Table 5) situated in or near three known SNRs: the Mon Loop, Shajn 147, and Vela. Each of the stars has a strong 2175 Å feature and a normal to high far-ultraviolet extinction (Fig. 6). With some qualifications, this pattern is the first consistent relationship found for extinction anomalies.

Of the stars in the Monoceros SNR (the Mon Loop), only HD 47240 is presently known to exhibit high-velocity gas in its line of sight; it also has the highest far-ultraviolet extinction of these stars. Wallerstein and Jacobsen (1976) did not find high-velocity Ca II toward HD 47129, HD 48099, or HD 48434; HD 46106 is in the Rosette nebula (NGC 2244), which is just outside the Mon Loop; HD 46711 is several degrees south of the loop. However, all of these stars are members of the Mon OB2 association, which is roughly centered on the Mon Loop. Turner (1976) finds that the youngest stars in Mon OB2 are concentrated in the Rosette nebula, while the older stars lie largely outside the Mon Loop. Singh and Naranan (1979) suggest that there may have been an older supernova in the same location that triggered the formation of these older stars. Whatever the exact sequence of events, it is clear that the gas and dust in the Monoceros region have been processed by one or more supernova blast waves. The expansion velocity of the Mon Loop itself is around 40–50 km $s^{-1}$ (Lozinskaya 1972).

The star HD 36665 in the Shajn 147 SNR does have high-velocity gas in its line of sight (Silk and Wallerstein 1973). This star has a noticeably strong 2175 Å feature, although the far-ultraviolet extinction is normal. The high-velocity Ca II line has a stronger component at low velocity with respect to the local standard of rest, so that some of the extinction features of the high-velocity gas may be obscured by a normal dust component.

TABLE 5

STARS ASSOCIATED WITH SUPERNOVA REMNANTS

| HD | Sp. | $E(B-V)$ | SNR | log $N$(H I)[a] | $N$(H I)/$E(B-V)$ |
|---|---|---|---|---|---|
| 36665 ... | B1 Ve | 0.65 | Shajn 147 | 21.43 | 4.1(21) |
| 46106 ... | B0.5 V | 0.42 | Mon Loop | 21.30 | 4.8(21) |
| 46711 ... | B3 Ib | 1.00 | Mon Loop | ... | ... |
| 47129 ... | O7.5 IIIf | 0.38 | Mon Loop | 21.18 | 4.0(21) |
| 47240 ... | B1 Ib | 0.40 | Mon Loop | 21.36 | 5.7(21) |
| 48099 ... | O7 V | 0.27 | Mon Loop | 21.20 | 5.9(21) |
| 48434 ... | B0 III | 0.28 | Mon Loop | 21.04 | 3.9(21) |
| 72350 ... | B5 IV | 0.14 | Vela | 21.15: | 1.0(22) |
| 75821 ... | B0 III | 0.09 | Vela | 20.48 | 3.4(21) |

[a]Column density of H I ($cm^{-2}$), from Bohlin, Savage, and Drake 1978 or Shull and Van Steenberg 1983.

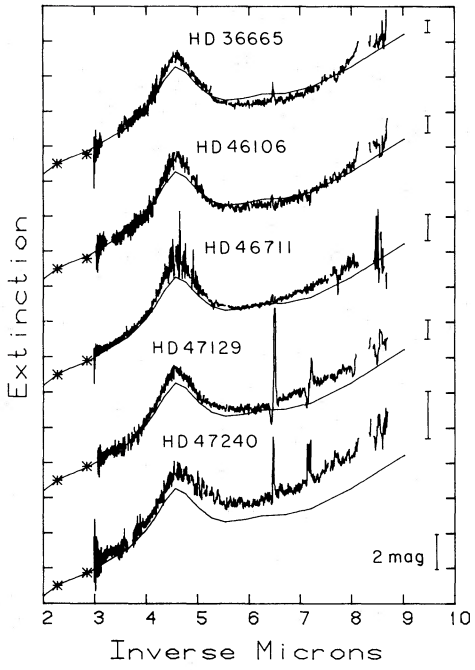


FIG. 6a

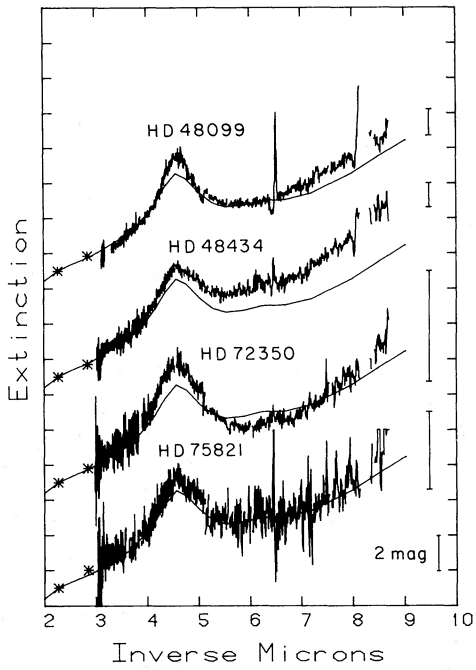


FIG. 6b

FIG. 6.—(*a*) and (*b*) Normalized $E(\lambda - V)/E(B - V)$ extinction curves toward nine stars associated with SNRs. Each curve is compared with the Savage and Mathis (1979) standard and is offset vertically by an arbitrary amount. Error bars give $\pm 1\ \sigma$ uncertainty in extinction at 1250 Å. HD 47129 is Plaskett's star.

The Vela SNR is the youngest SNR of the three and has the highest expansion velocity (Silk and Wallerstein 1973). Both HD 72350 (Jenkins *et al.* 1981) and HD 75821 (Jenkins, Silk, and Wallerstein 1976) have high-velocity gas in the line of sight. Jenkins *et al.* (1981) characterize the whole region, including the Gum nebula, as having very little dust [HD 72350 and HD 75821 are reddened by only $E(B - V) = 0.16$ and 0.09]. The very small degree of reddening for the latter star makes its $E(B - V)$ normalized ultraviolet extinction curve very noisy. The HD 72350 curve is cleaner and shows a very strong 2175 Å feature and somewhat higher far-ultraviolet extinction.

These extinction curves are in general agreement with the shock-processing calculations, particularly with regard to the strength of the 2175 Å bump. The prediction of high far-ultraviolet extinction is less well matched, although it is significant that none of these stars have low far-ultraviolet extinction. Total hydrogen column densities are available for some of these stars from Lyman-$\alpha$ profile fitting using high-dispersion *IUE* data. These values are shown in Table 5 along with the ratio $N(\text{H I})/E(B - V)$. This ratio is higher than the mean interstellar value of $4.8 \times 10^{21}$ cm$^{-2}$ mag$^{-1}$ (Bohlin, Savage, and Drake 1978) for only three stars. However, the interpretation of both the extinction curves and the gas-to-dust ratios is complicated by possible admixtures of unprocessed foreground dust, particularly in the lightly reddened Vela stars. The other stars all show low-velocity gas components that might affect the total extinction properties. Quantitative agreement with the modeling results is therefore not expected.

The pattern of extinction properties for these stars supports the MRN grain model, which attributes the 2175 Å bump to graphite. The metallic oxide surface reaction theory (Duley, Millar, and Williams 1979, and references therein) might also lead to a strengthening of this bump. This alternate theory says that the 2175 Å feature is due to $O^{2-}$ ions in crystal sites with coordination number four (the coordination number in a perfect MgO crystal is six). MacLean, Duley, and Millar (1982) note that such sites will occur on the surface of grains or can be produced by stress or high-energy irradiation (Sibley, Kolopus, and Mallard 1969). The motion of the grain through the postshock gas which leads to nonthermal sputtering could produce additional low-coordination $O^{2-}$ sites, thereby strengthening the 2175 Å feature. However, the same irradiation would produce additional $O^{2-}$ sites with coordination number three. These sites should give absorption near 2700 Å (Millar 1981). The data show that the 2175 Å bump is strengthened, but there is little evidence for a 2700 Å feature. Therefore, the observations presented here do not support the metallic oxide grain theory. However, MacLean, Duley,

and Millar (1982) note that the 2700 Å feature appears only in highly activated MgO samples and is about one-tenth as strong as the 2175 Å feature. Since it falls in the nosiest portion of the extinction curves, a weak feature could be present at 2700 Å. Some further analysis of the surface effects of particle bombardment on grains in shocks is needed to decide how strongly the present results argue against the metallic oxide grain theory.

## VI. SUMMARY

Theoretical modeling of shock processing of grains indicates that the ultraviolet extinction curve of these grains will show stronger 2175 Å bumps and high far-ultraviolet extinction. Significant grain destruction occurs for shock speeds as low as 40 km $s^{-1}$. At $V_s \sim 100$ km $s^{-1}$, about 50% of the silicate grain material is returned to the gas phase, but only 15% of the graphite material is returned. These results should be regarded as qualitative indications of the pattern of grain destruction, since there are major approximations made in the construction of a grain model, the treatment of grain-grain collisions, and the small Larmor radius treatment of the grain dynamics. For the assumptions made, the results are only about 20% sensitive to the choices of grain parameters.

The changes in extinction curves result from the greater destruction of silicate grains compared to graphite, and from the greater destruction of large grains. The latter result depends on the choice made for a cutoff on the small Larmor radius approximation. Other than this, the strong bump and high far-ultraviolet extinction follow necessarily from the MRN grain model.

Observations of extinction curves for stars behind SNRs generally support the model results. All nine of the observed stars have strong 2175 Å extinction features and normal to high far-ultraviolet extinction. While this pattern could potentially be explained by the metallic oxide grain theory as well, the absence of an extinction feature at 2700 Å for these stars argues against this theory. Optical diffuse band strengths would show similar correlations with SNR activity, if these bands were carried by a population of large grains. However, the preliminary studies by Snow, Timothy, and Saar (1982) suggest that diffuse bands may be created by a population of very small, and therefore hardy, grains.

We thank Dr. T. P. Snow for numerous discussions on the subject of grain extinction and Dr. D. Hollenbach for comments on the manuscript. This work was supported by NASA/*IUE* grants NAG5-193 and NSG-5300, and NSF grant AST 82-16481 at the University of Colorado.

## REFERENCES

Barlow, M. J. 1978, *M.N.R.A.S.*, **183**, 367.
Biermann, P., and Harwit, M. 1980, *Ap. J.* (*Letters*), **241**, L105.
Bohlin, R. C., Savage, B. D., and Drake, J. F. 1978, *Ap. J.*, **224**, 132.
Cowie, L. L. 1978, *Ap. J.*, **225**, 887.
Draine, B. T., and Salpeter, E. E. 1979, *Ap. J.*, **231**, 77.
Duley, W. W., Millar, T. J., and Williams, D. A. 1979, *Ap. Space Sci.*, **65**, 69.
Harris, D. H., Woolf, N. J., and Rieke, G. H. 1978, *Ap. J.*, **226**, 829.
Hollenbach, D., and McKee, C. F. 1979, *Ap. J. Suppl.*, **41**, 555.
Jenkins, E. B., Silk, J., and Wallerstein, G. 1976, *Ap. J.* (*Letters*), **209**, L87.
Jenkins, E. B., Silk, J., Wallerstein, G., and Leep, E. M. 1981, *Ap. J.*, **248**, 977.
Jorgenson, G. V., and Wehner, G. K. 1965, *J. Applied Phys.*, **36**, 2672.
Lozinskaya, T. A. 1972, *Soviet Astr.—A.J.*, **15**, 910.
MacLean, S., Duley, W. W., and Millar, T. 1982, *Ap. J.* (*Letters*), **256**, L61.
Mathis, J. S., Rumpl, W., and Nordsieck, K. H. 1977, *Ap. J.*, **217**, 425 (MRN).
McCray, R. A., and Snow, T. P. 1979, *Ann. Rev. Astr. Ap.*, **17**, 213.
McKee, C. F., and Ostriker, J. P. 1977, *Ap. J.*, **218**, 148.
Meyer, D. M., and Savage, D. B. 1981, *Ap. J.*, **248**, 545.
Millar, T. J. 1981, *Ap. Space Sci.*, **72**, 509.
Morton, D. C. 1974, *Ap. J.* (*Letters*), **193**, L35.
_____. 1975, *Ap. J.*, **197**, 85.
Nandy, K., Thompson, G. I., Jamar, C., Monfils, A., and Wilson, R. 1976, *Astr. Ap.*, **51**, 63.
Savage, B. D., and Mathis, J. S. 1979, *Ann. Rev. Astr. Ap.*, **17**, 73.
Shull, J. M. 1977, *Ap. J.*, **215**, 805.
_____. 1978, *Ap. J.*, **226**, 858.
Shull, J. M., and McKee, C. F. 1979, *Ap. J.*, **227**, 131.
Shull, J. M., Seab, C. G., and McKee, C. F. 1983, in preparation.
Shull, J. M., and Van Steenberg, M. 1983, in preparation.
Shull, J. M., York, D. G., and Hobbs, L. M. 1977, *Ap. J.* (*Letters*), **211**, L139.
Sibley, W. A., Kolopus, J. L., and Mallard, W. C. 1969, *Phys. Stat. Solids*, **31**, 223.
Sigmund, P. 1969, *Phys. Rev.*, **184**, 383.
Silk, J., and Wallerstein, G. 1973, *Ap. J.*, **181**, 799.
Singh, K. P., and Naranan, S. 1979, *Ap. Space Sci.*, **66**, 191.
Snow, T. P., Timothy, J. G., and Saar, S. 1982, *Ap. J.*, **262**, 611.
Spitzer, L. 1976, *Comments Ap.*, **6**, 157.
Turner, D. G. 1976, *Ap. J.*, **210**, 65.
van de Hulst, H. C. 1957, *Light Scattering by Small Particles* (New York: Wiley).
Wallerstein, G., and Jacobsen, T. S. 1976, *Ap. J.*, **207**, 53.

C. GREGORY SEAB: NASA Ames Research Center, MS 245-6, Moffett Field, CA 94035

J. MICHAEL SHULL: Joint Institute for Laboratory Astrophysics, University of Colorado, Campus Box 440, Boulder, CO 80309